7th High Performance Yacht Design Conference
Auckland, 11-12 March 2021

FORCE GENERATION MECHANISMS OF DOWNWIND SAILS

Abel Arredondo-Galeana[1], abel.arredondo-galeana@strath.ac.uk
Ignazio Maria Viola[2], I.M.Viola@ed.ac.uk

Abstract. The force generation mechanisms of a yacht sail are discussed with the aid of force and flow measurements on a model scale spinnaker. The velocity and vorticity fields are measured on five horizontal sections with particle image velocimetry. By comparing the forces measured with a balance to those computed from the vorticity field, we demonstrate how the force generation can be interpreted by the production and stretching of vortex rings. We consider vortex rings to be continuously generated and shed from the perimeter of the sail. The intersection of their vertical legs with horizontal planes are leading and trailing edge vortices. The sail force is due to the rate of change of the impulse of the vortex rings. Consequently, we show that the force can be computed from the time-averaged vorticity field using the Kutta-Joukowski lift formula, or from the strength and relative velocity of the leading and trailing edge vortices, or from the vorticity flux at the perimeter of the sail. The drag is estimated with Filon's drag formula. These results confirm experimentally the theoretical work of Viola et al. [1] and pave the way to the development of design methodologies that improve sail performance by manipulating the local vorticity field.

1. NOMENCLATURE

α	Sectional angle of attack
$\beta_{a\mathrm{OPT}}$	Optimum apparent wind angle
δ	Twist
Γ^-	Time averaged circulation of leading edge vortex
Γ^+	Time averaged circulation of trailing edge vortex
Γ_{LE}	Circulation of leading edge vortex
Γ_{TE}	Circulation of trailing edge vortex
$\dot{\Gamma}_{LE}$	Vorticity flux at leading edge
$\dot{\Gamma}_{TE}$	Vorticity flux at trailing edge
η	Rotational or trim angle
ρ	Density of fluid
ω_z	Spanwise vorticity
A	Area of sail and initial surface area of vortex ring
$\dot{A}$	Rate of change of vortex ring surface area
A_b	Area of bound vortex ring
C_{DF}	Drive force coefficient
$C_{DF,\max}$	Maximum force coefficient
c	Sectional chord length
c_0	Average chord length
I	Impulse
L	Lift force
D	Drag force
L_{LE}	Vorticity flux integration line at leading edge
L_{TE}	Vorticity flux integration line at trailing edge
V_a	Apparent wind
V_b	Boat velocity
V_t	True wind velocity
Re	Reynolds number
S	Span
t^*	Non-dimensional time
U_{LE}	Velocity of leading edge vortex
U_{TE}	Velocity of trailing edge vortex
U_∞	Freestream velocity
W	Integration line for drag computation
LEV	Leading edge vortex
TEV	Trailing edge vortex
PIV	Particle Image Velocimetry
x, y, z	Streamwise, normal, spanwise direction

2. INTRODUCTION

Downwind sails such as spinnakers are between the most powerful sails carried by a sailing yacht. However, the force generation mechanisms have often been incorrectly identified. In fact, these sails have a sharp leading edge that promotes flow separation. The bound circulation, intended as the net integral of vorticity in the thin Prandtl's boundary layer, is negligible to generate a negative lift. Hence, it cannot be the origin of the aerodynamic force [2,3]. Viola et al. [1] showed theoretically that the force generated by a sail is due to the production and stretching of vortex rings. In this paper we demonstrate this theory with physical experiments on model scale spinnakers. We show that the main force generation mechanism is associated with the convection velocity of the leading and trailing edge vortices, or by the production of vorticity that enables the associated vortex rings to grow in size. Here, we interpret the shedding vortices as the intersections of a vortex ring with a horizontal plane. We also show that the relative velocity of the leading and trailing edge vortices results, in the time average sense, in bound circulation and thus enables using the Kutta-Joukowski lift formula.

Twist of the onset flow and the sail geometry are not expected to affect the deformation and stretching of the vortex rings, but only their initial shape. We note however that non-axisymmetric vortex rings, like the ones pinched-off from a spinnaker are not in equilibrium and would probably change shape while convecting downstream [4].

3. METHODOLOGY

3.1. Sailing Conditions

In the laboratory setting, where the boat is fixed with respect to the water tunnel, the free stream represents the apparent wind $\boldsymbol{V_a}$. Hence, the sail must be set at the corresponding optimum apparent wind angle ($\beta_{a\mathrm{OPT}}$), which is the angle between the apparent wind $\boldsymbol{V_a}$ and the boat velocity $\boldsymbol{V_b}$. This angle varies with the height and thus is taken at a nominal height of 10 m. In fact, the boat

[1] Postdoctoral Research Associate, Department of Naval Architecture, Ocean & Marine Engineering, University of Strathclyde, UK
[2] Reader, School of Engineering, Institute for Energy Systems, University of Edinburgh, UK

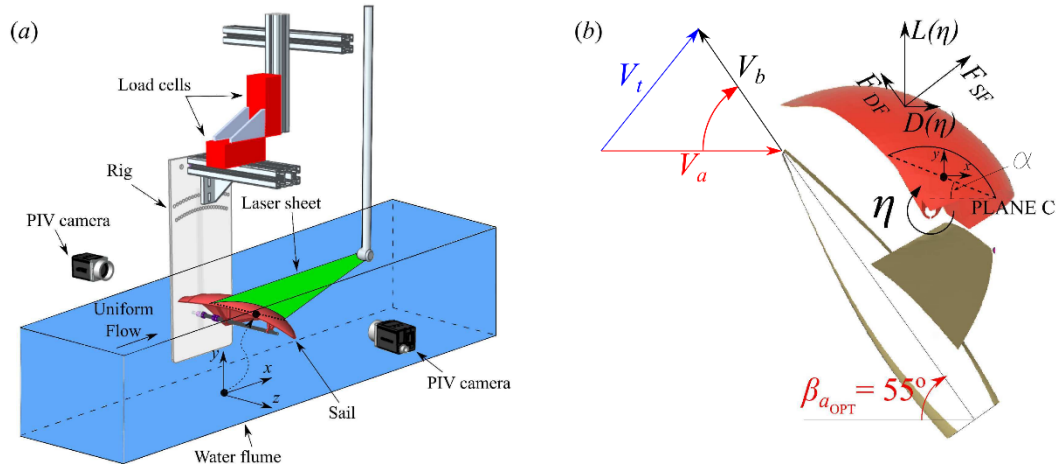

Figure 1. (a) Experimental setup in the water tunnel, where the sail is rotated by $\pi/2$ around the x-axis compared to the real sailing conditions and (b) Sail S_1 at $\beta_{a_{OPT}}$ as it would appear with respect to a boat hull from a bird's eye view

sails in the atmospheric boundary layer and thus the boat experiences an apparent wind velocity that is $\boldsymbol{V_a(z) = V_t(z) - V_b}$. The spinnaker considered in this paper was designed for $\beta_{aOPT} = 55^{\circ}$.

3.2. Sailing Geometry

The sail geometry was designed for the AC33 class yachts. This class, which is a set of rules for the design of the boat and the sails, was proposed for the 33rd America's Cup. The America's Cup is the world's oldest trophy and one of the most prestigious yacht races. The AC33 class was never adopted because of a legal dispute between the Defender, Alinghi, and the Challenger, Oracle BMW. Hence, the 33rd America's Cup was eventually sailed by multi-hulls under the conditions set by the Deed of Gift instead of a class rule. However, the aerodynamics of this spinnaker has been widely investigated in the last decade [5,6,7,8] and this makes it one of the best available benchmarks for downwind sails. The sail geometry together with useful notes on the spinnaker are available on https://voilab.eng.ed.ac.uk.

The original sail was designed to be 34 m in span, with a sail area of 510 m^2, while here a 1:100th scale model is considered. The particle image velocimetry (PIV) measurement planes were located at 7/8th, 5/6th, 3/4th, 1/2th and 1/4th the distance from the bottom of the sail to its tip, and labelled as planes A, B, C, D and E, respectively. We note that plane E is above the clue. A solid model was 3D printed in ABS. The sail had a span (S) of 300 mm, an area (A) of 0.045 m^2, an average chord length ($c_0 = A/S$) of 150 mm, an average thickness of 3 mm and a bevel angle at the leading edge of 20°. The twist from head to foot was $\delta = 16^{\circ}$. A 2% thickness is negligible on the sail aerodynamics, particularly because the leeward and windward sides of each sail section are parallel to the camber line. However, the leading-edge shape is critical for the direction of the separating streamline. To minimise this effect, we adopted the minimum sail thickness and bevel angle compatible with structural requirements [2].

3.3. Water tunnel setup

Figure 1a shows the experimental setup. The water tunnel is located at the University of Edinburgh. It is 9 m long and 0.4 m wide, with a flat, horizontal bed. The mean water depth was set to 0.5 m. The mean flow speed over the area occupied by the model was $U_\infty = 0.14\ \mathrm{ms}^{-1}$. With a span of 0.3 m, this results in a Reynolds number $Re = 2 \times 10^4$. Assuming a full-scale wind speed of $5\ \mathrm{ms}^{-1}$, Re is 4×10^{-3} times smaller than at full-scale. Despite this significant difference between model and full scale Re, the differences in the flow field are expected to be moderated because the flow is fully separated at the sharp leading edge. In fact, the dynamics of leading-edge and trailing-edge vortices is only marginally affected by changes in the Reynolds number within the range from 10^4 to 10^6 [9,10].

The sail model was mounted and rotated by $\pi/2$ in the water tunnel, i.e. the water plane of the model-scale sail was parallel to a vertical sidewall of the water tunnel. A right-handed coordinate system is defined at the centre of the chord of plane C, as shown in figure 1a. The x- and y-coordinates are the streamwise and vertical directions, respectively. The sail model orientation could be adjusted by a rotation around a shaft parallel to the z-axis. The rotation is defined as the trim angle η (figure 1b). Here, $\eta = 0^{\circ}$ when the driving force is maximum.

The experiments were carried with the spinnaker in isolation. We assume that the main effect of the mainsail is to generate a uniform upwash variation of the angle of attack experienced by the spinnaker. We account for this by testing at different η. However, if we had tested with a mainsail, the mainsail circulation would deflect the spinnaker wake, resulting in potentially more attached flow in the results presented in the following sections.

3.4. Load cells

The load cells used in the experiments comprised a wind tunnel lift and drag dual-balance kit manufactured by KineOptics. The kit consisted of two Honeywell strain

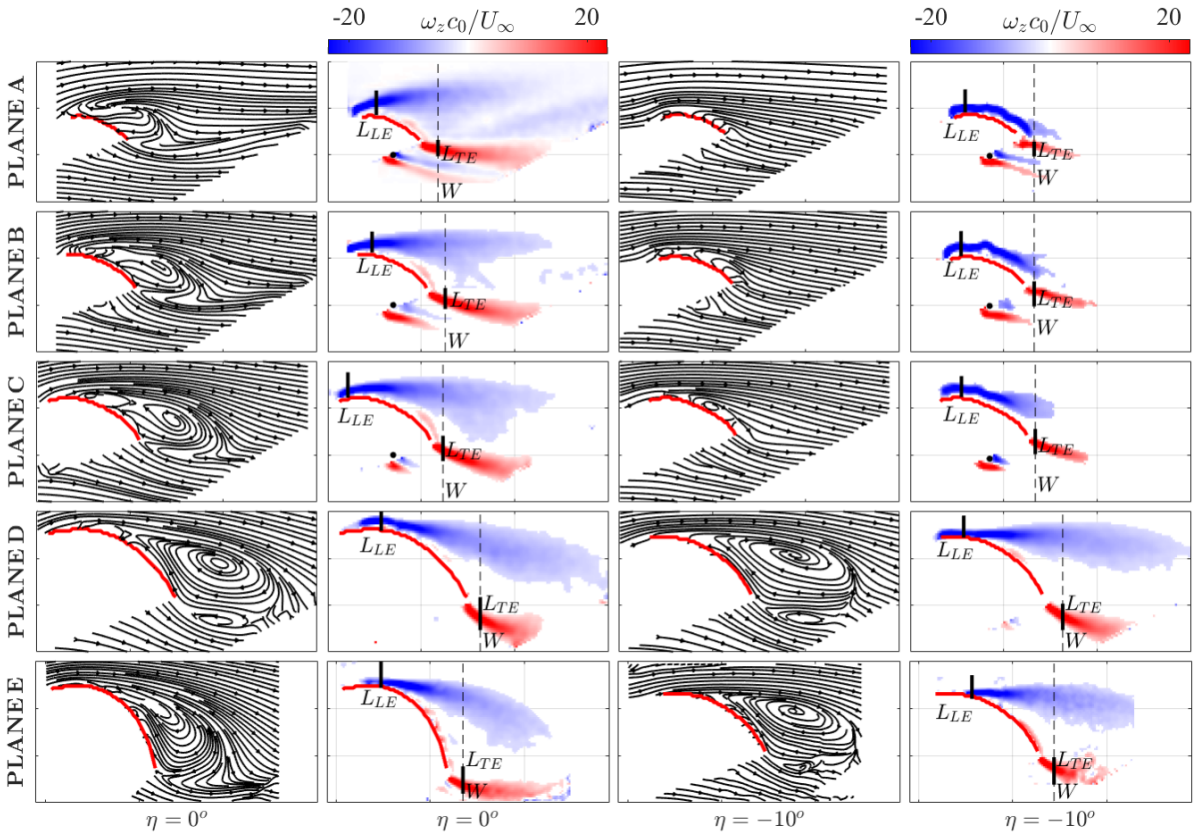

Figure 2. Time-averaged near-wake streamlines and nondimensional vorticity contours for the optimal sail trim in light wind conditions ($\eta = 0^\circ$, two left columns) and a depowered trim for strong wind conditions ($\eta = -10^\circ$, two right columns). The lines L_{LE} and L_{TE} are used in §4.6 to integrate the vorticity flux, while the dashed line W is used in §4.7 to compute the drag force

gauges connected to two SGA/A amplifiers. A low pass filter was set to 5 Hz to reduce high frequency noise coming from vibrations of the belt driving the flume propeller or electric noise. The excitation voltage for the strain gauges was 10 volts DC and 5 volts DC, for the lift and drag gauges, respectively. The amplifiers used a power voltage of 18-25 volts DC. The output analogue signals of the amplifiers were converted to digital signals, with a 16-bit National Instruments 6259 A/D board. Force signals were recorded with Wavelab.

3.5. Particle Image Velocimetry

PIV measurements were performed across *x*-*y* planes parallel to the free stream. The PIV system consisted of a Solo 200XT pulsed dual-head Nd:YAG laser, with an energy output of 200 mJ at a wavelength of λ = 532 nm. The laser beam was converted into a laser sheet through an array of underwater LaVision optics. The optics were fully submerged and created a laser sheet with a thickness of approximately 2 mm. The camera was a CCD Imperx 5MP with a 2448 px × 2050 px resolution and a Nikkor f/2, 50 mm lens. Seeding particles were silver coated hollow glass spheres, with an average diameter of 14 μm and a density of 1.7 g/cc. PIV image pairs were sampled at 7.5 Hz and a two-pass adaptive correlation was applied. The first pass had a 64 px × 64 px interrogation window, with a Gaussian weighting and 50% window overlap. The second pass had a 24 px × 24 px interrogation window and a 75% window overlap. Finally, a 3 × 3 Gaussian filter was used to smooth the vector fields. In order to mitigate surface reflections, a coating of matt black paint doped with rhodamine B was applied to the sail surface, allowing a notch filter on the camera to subtract the wavelength of rhodamine B and minimise the reflected light. A second coating of acrylic was applied to protect the rhodamine from dissolving in water. Additionally, background subtraction removed prevailing reflections and enabled measurements near the wall. The leading-edge region was not affected by laser reflections due to the curvature of the sail and the direction of the laser sheet. Successful background subtraction showed that no discernible deformation of the sail or strut occurred during the experimental runs. The strut was made of steel and designed with a thick root and then stepped down into a slimmer section in order to minimise deflections.

4. RESULTS

4.1. Time-averaged vorticity fields for different flow conditions

Figure 2 shows the near wake of the sail. Time- averaged streamlines and contours of nondimensional spanwise vorticity ($\omega_z\, c_0/U_\infty$) are presented for two trim angles, $\eta = 0^\circ$ and $\eta = -10^\circ$. These two angles are selected because the sail trim that allows $C_{DF,\max}$ ($\eta = 0^\circ$) is likely to be optimal in low wind speed conditions. Conversely,

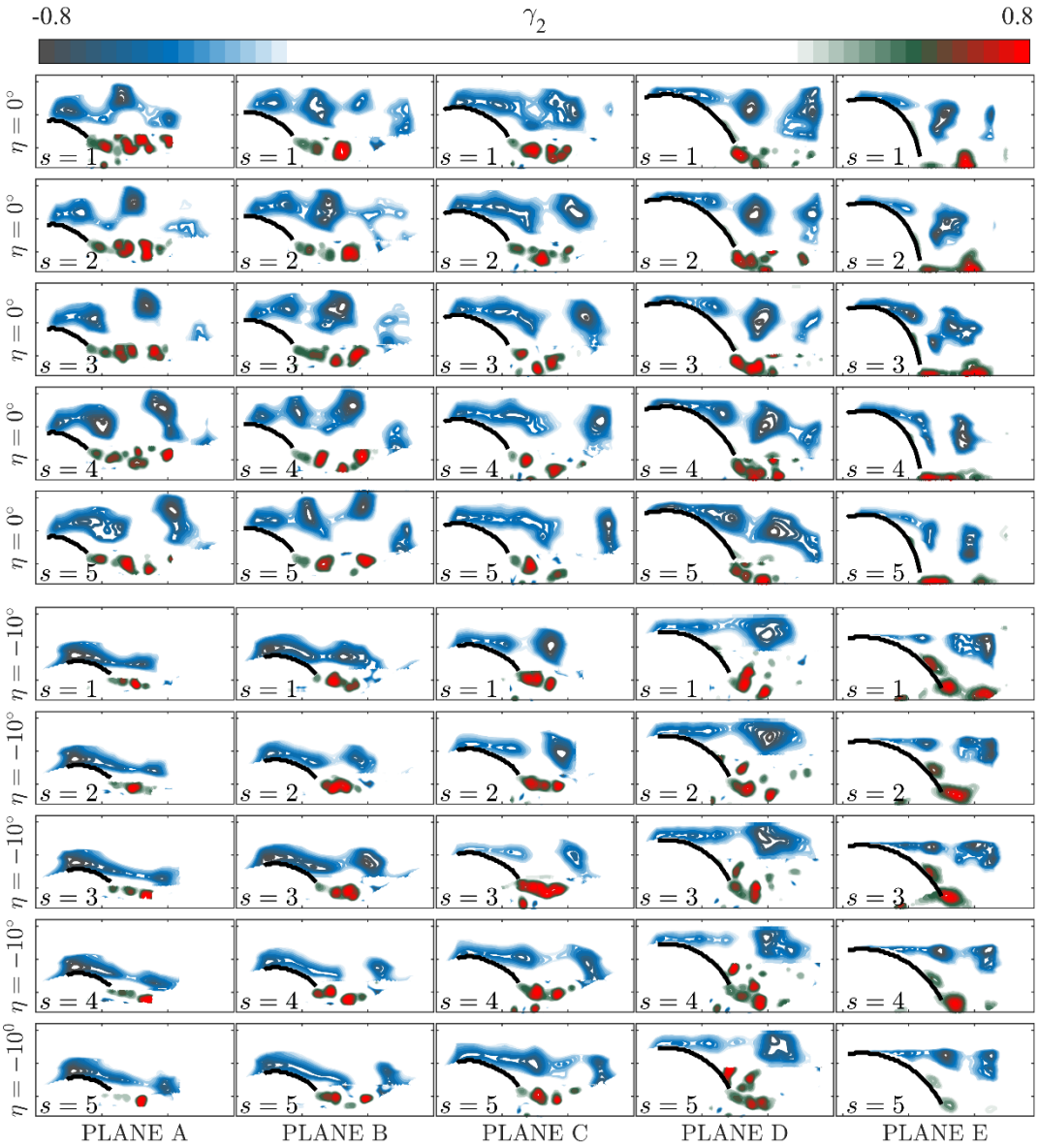

Figure 3 Sequence of γ_2 contours of sail S_1 based on vorticity measurements taken at five consecutive time steps (s = 1-5) on planes A, B, C, D and E (columns 1-5, respectively) at $\eta = 0^\circ$ (top array) and $\eta = -10^\circ$ (bottom array)

in strong wind conditions, the optimal trim is one that provides a reduced side force coefficient (C_{SF}), which increases the hydrodynamic resistance of the boat. Hence, there is a wind condition, which depends on the hydrodynamic performance of the boat, such that the optimal trim is $\eta = -10^\circ$.

Five flow fields are presented in figure 2, corresponding to the five PIV measurement planes (A, B, C, D, E) along the span of the sail. In the figure, plane A is the closest to the head and plane E the closest to the bottom of the sail and above the clue. A total of 500 images are averaged per plane. The lines L_{LE} and L_{TE}, in the vorticity plots of figure 2, are used in §4.6 to integrate the vorticity flux and the vorticity moment. Whilst the dotted line W is an integration line that is utilised to estimate the drag force in §4.7.

The light wind condition $\eta = 0^\circ$ is shown on the two left columns of figure 2. The streamlines of figure 2 reveal a large time-averaged recirculation region in most of the planes. Following the definitions of Perry & Steiner [8], stable foci are observed at the centre of the circulation regions, indicating the tridimensionality of the flow field. At the head of the sail at $\eta = 0^\circ$, a bifurcation line appears in plane A at the centre of the recirculation region. Contrarily, it is noted that near midspan of the sail, such as in plane D and at $\eta = 0^\circ$, two-dimensional nodes appear at the centre of the recirculation region.

In stronger breeze, at $\eta = -10^\circ$, a stable node near the surface of the sail is noted on the mid plane C. Conversely, in planes A and B, the streamline patterns close to the surface of the sail are c-shaped and indicative of vortex shedding. Perry and Steiner [8], for example, showed this

same pattern behind the wake of a bluff body when the train of leading and trailing-edge vortices came in close proximity to each other.

The vorticity-contours identify two opposite sign circulation areas in all of the planes and at both $\eta = 0^{\circ}$ and $\eta = -10^{\circ}$, with negative vorticity emerging from the leading-edge and positive vorticity from the trailing-edge. On the highest sections, the positive (red) and negative (blue) vorticity wakes of the strut (indicated by a black dot) are also visible on the windward side of the sail section.

At $\eta = 0^{\circ}$, the highest sections of the sail (planes A, B and C) are stalled resulting in a large trailing-edge wake. Conversely, at $\eta = -10^{\circ}$, vorticity mostly follows the sail profile. It is to note that the bottom sections (planes D and E) are stalled at both angles η.

On any plane, there is more negative vorticity than positive vorticity. We will show in §4.5 that this is because of slower advection of negative leading-edge vorticity than of positive trailing edge vorticity. Because the time-averaged vorticity distribution is fixed with respect to the sail, the net vorticity (i.e. the sum of positive and negative vorticity) is the bound vorticity intended by Kutta [11] and Joukowski [12]. The bound circulation will be computed in §4.4 and it will be compared to that required to get the experimentally measured lift force.

4.2. Instantaneous vorticity field

The instantaneous vorticity field is investigated with a data set of 500 images, from which a subset of 5 images is presented in figure 3. To identify coherent regions of co-sign rotating flow, the γ_2-criterion [13] is used. The full data set of instantaneous flow fields is available in the supplementary material on the Edinburgh DataShare repository (datashare.is.ed.ac.uk). Each image is sampled at 7.5 Hz, corresponding to a non-dimensional convective time period $t^* = tU_\infty/c_0 = 0.13$. The instantaneous flow fields are shown in figure 3 for planes A-E at $\eta = 0^{\circ}$and $\eta = -10^{\circ}$. Each instantaneous image is labelled with an index s, where s indicates the sequence number of the image. It should be recalled that the 5 planes were not recorded simultaneously.

The γ_2-criterion enabled the identification of vortex structures. As anticipated by the analysis of the time-averaged flow field topology in §4.1 vortex shedding occurred in all of the planes. Closed γ_2 isolines formed at the leading and trailing edges identify leading-edge vortices (LEVs) and trailing-edge vortices (TEVs), respectively. Both LEVs and TEVs are continuously generated and shed downstream.

The LEV is a more coherent vortex structure than the TEV, which instead shows a more stretched vorticity distribution in the streamwise direction. This difference is also associated with a slower streamwise velocity of the LEV. Near the sail, the LEV convects roughly at $U_\infty/2$ (see figure 3, plane D at $\eta = 0^{\circ}$), whilst away from the sail it convects at U_∞ (see figure 3, plane A at $\eta = 0^{\circ}$). The TEV convects at U_∞, both near and away from the sail, as estimated by Stevens et al. [14]. It will be shown in §4.4 that this results in about twice the integral of negative time-averaged vorticity over the entire field of view than the positive one.

4.3. Impulse theory formulae

The force production mechanisms can be described using impulse theory. For a volume of fluid V_f with constant density ρ, whose external boundaries approach infinity,

$$F = -\int_{V_f} \rho \frac{d\boldsymbol{u}}{dt} dV = -\rho \frac{d}{dt} \int_{V_f} \boldsymbol{u} dV = -\rho \frac{d\boldsymbol{I}}{dt}, \quad (1)$$

where

$$\boldsymbol{I} = \int_{V_f} \boldsymbol{u} dV \quad (2)$$

is the impulse. Wu [15] and Lighthill [16] showed that the impulse is given by the sum of the integral over the fluid volume V_f of the first moment of the vorticity ω, and the integral over the volume surface S_b with outward unit normal $\boldsymbol{n}$ of the moment of tangential velocity:

$$\boldsymbol{I} = \frac{1}{n_d - 1} \left(\int_{V_f} \boldsymbol{x} \times \boldsymbol{\omega} dV + \int_{S_b} \boldsymbol{x} \times (\boldsymbol{n} \times \boldsymbol{u})\, dS \right), \quad (3)$$

where $n = 2$ and 3 in two and three dimensions, respectively, and $\boldsymbol{x} = (x, y, z)$ is the coordinate vector. A complete derivation and discussion is available in, for instance, Eldredge [17] (p. 190). The second term of eq. 3 vanishes in a reference system fixed with the body. This, in fact, is an unsteady body force equal to the difference between the forces as observed from the reference system $O(x, y, z)$ and those observed from a reference system fixed with the body. It is proportional to the mass of the body [18,19] and thus its effect is negligible for slender bodies with small volume to surface area ratio [20] and for small body to fluid density ratio [21].

Assuming a tridimensional model, as the one considered here, and a reference system fixed with the sail in eq. 3, eq. 1 becomes

$$F = -\frac{\rho}{2} \frac{d}{dt} \int_{V_f} \boldsymbol{x} \times \boldsymbol{\omega} dV. \quad (4)$$

Let us consider the vorticity field as made of the sum of discrete vortex rings, each with a strength Γ_j, minimum surface area spanned by the vortex loop A_j, and unit vector $\boldsymbol{n}_j$ normal to the surface and pointing in the opposite direction to the surface induced velocity of the vortex ring, which acts orthogonal to its surface. The impulse of a vortex ring, which was first found by Lamb [22], is $\rho\Gamma A$. Hence, eq. 4 can be written as [14],

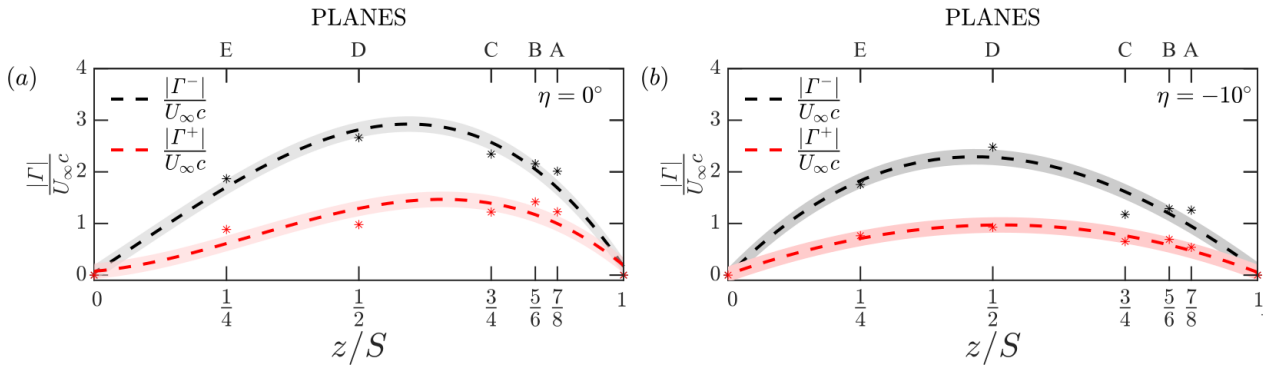

Figure 4. Nondimensional leading-edge circulation $\Gamma^-/U_\infty c$ and trailing-edge circulation $\Gamma^+/U_\infty c$ versus the spanwise nondimensional coordinate z/S for (a) $\eta = 0^\circ$ and (b) $\eta = -10^\circ$. Markers indicate measured data, whilst dotted lines are third-order polynomial fits with shaded regions showing the 95% CI of the fit.

$$F = \frac{\rho}{2}\sum_j (\dot{\Gamma}_j A_j + \Gamma_j \dot{A}_j)\boldsymbol{n}_j. \quad (5)$$

4.4. Bound vorticity

In this section, the time-averaged vorticity field is interpreted as a vortex ring bound to the sail. The ring is made by the net vorticity shown in the near wake of the sail (figure 2), the tip vortices and the starting vortex. Later on, in §4.5, discrete vortex rings are considered, whose cross-sections are the leading and trailing edge vortices from the instantaneous flow field.

Here, let us assume the vorticity as forming a single bound vortex ring with circulation $-\Gamma_b$ and a surface area A_b. Because this hypothetical vortex ring at steady state is long due to the starting vortex being at infinity, the surface of the ring is orthogonal to the y axis and thus the computed force will act in the lift direction.

The rate of change of the surface area of the vortex ring is $\dot{A}_b = SU_\infty$. We recall that S is the span, whilst $-\dot{\Gamma}_b$ is the production of the circulation needed to lengthen the tip vortex with strength $-\Gamma_b$ at a rate U_∞. Hence $-\dot{\Gamma}_b A_b = -\Gamma_b S U_\infty$. Substituting into eq. 5, we find the Kutta-Joukowski lift formula

$$L = -\rho S U_\infty \Gamma_\mathrm{b}. \quad (6)$$

As mentioned in the previous section, in the time-averaged vorticity field, the net vorticity on each plane is the bound circulation Γ_b. An integral value of the bound circulation is given by:

$$\Gamma_\mathrm{b} = \frac{1}{S}\int_S (\Gamma^- + \Gamma^+)dz, \quad (7)$$

where Γ^- and Γ^+ are the total negative and positive time-averaged circulations in the field of view of figure 2.

The circulation around the time-averaged leading and trailing-edge circulation zones is computed from the (discrete) area integral of vorticity. Vorticity is thresholded above the measurement uncertainty level to avoid accumulation of low-level vorticity in the results. The circulation is nondimensionalised and plotted in Figures 4a and 4b, for every plane and for the two trim angles η. The marks show the measured circulations, whilst the spanwise circulation distributions are approximated with third order polynomials showed by dotted lines. The area under the Γ^- distribution is approximately twice of that under Γ^+ for both of the trim angles η. By using the fitted curves in Fig. 4, the bound circulation is $0.9U_\infty c$ at $\eta = 0^\circ$ and $0.73U_\infty c$ at at $\eta = -10^\circ$. These values are 4% and 12% greater, respectively, than those measured with the load cells. Force comparisons with wind tunnel measurements are difficult since it is not known whether the maximum driving force trim angle ($\eta = 0^\circ$) between this experiment and wind tunnel tests of spinnakers in isolation is the same. At maximum driving force, the measured lift coefficient here was $C_L = 1.3$, whilst according to CFD studies [5], it could be $C_L = 1.6$. Differences can be attributed to the mainsail upwash which rotates the effective lift and drag axes and higher Reynolds numbers.

The comparison between Fig. 4a and 4b shows that, when the sail is depowered (from $\eta = 0^\circ$ to $\eta = -10^\circ$), the bound circulation decreases almost uniformly along the span of the sail by a proportional reduction of both positive and negative vorticity.

4.5. Vortex force

An alternative approach to use the time-averaged vorticity field as in the previous section, is to compute the vortex force based on the relative velocity of the leading and trailing edge vortices. In steady conditions, the same amount of positive and negative vorticity is shed into the wake. Hence, for every LEV, it is possible to identify a region whose integral of vorticity is opposite to the LEV circulation. Because the LEV and the TEV advect at different velocities, more leading-edge vorticity than trailing-edge vorticity is observed on average near the sail. This occurs only in the near wake though. In fact, in the far wake, positive and negative vorticity must convect at

the same velocity to ensure that the net time-averaged vorticity vanishes in accordance with Kelvin's theorem. The instantaneous vorticity fields can be interpreted as made of vortex rings, where each LEV-TEV pair in planes A-E are the intersection of one ring with the planes. The surface A_j of the vortex ring is the distance between the LEV and the TEV, integrated over the span S. It is worth noting that, chosen the jth LEV, the choice of the corresponding jth TEV to form a vortex ring is arbitrary, as long as the sum of their circulations is null ($\Gamma_{\mathrm{LEV}_j} + \Gamma_{\mathrm{TEV}_j} = 0$).

Let us now consider the two force production mechanisms in eq. 5. The surface of the jth vortex ring with positive circulation $\Gamma_j = -\Gamma_{\mathrm{LEV}j}$ stretches in the streamwise direction at a rate $\dot{A}_j = S(U_{\mathrm{TEV}j} - U_{\mathrm{LEV}j})$. The force associated with the streamwise stretching of the vortex enclosed surface is in the lift direction. Only n vortex rings within the near wake stretch at a rate $\dot{A}_j$, because U_{LEV} gradually increases to the same velocity as U_{TEV}. Hence, only n vortex rings can be considered. To estimate the force due to the rate of production of vorticity, let us consider the circulation needed to lengthen (in the streamwise direction) the area enclosed by the vortex ring. Akin to the consideration made to derive the Kutta-Joukowski lift formula in §4.4, here we find that $\dot{\Gamma}_j A_j = \Gamma_j \left(U_{\mathrm{TEV}_j} - U_{\mathrm{LEV}_j}\right) S$. Hence the two terms between parentheses on the right hand side of eq. 5 are identical and by substitution

$$L = -\rho \int_S \sum_j^n \left(U_{\mathrm{TEV}_j} - U_{\mathrm{LEV}_j}\right) \Gamma_{\mathrm{LEV}_j} \mathrm{d}z. \quad (8)$$

An equivalent formulation for the lift of a flat plate based on the relative velocity of the LEV and TEV was derived by Stevens et al. [14].

This formulation is equivalent to that in eq. 6 and 7 as can be shown by comparing the sectional lift computed with the two approaches. Assume for example, n LEVs convecting downstream at kU_∞ while the TEVs convect with velocity U_∞, and the same circulation for both LEVs and TEVs since they both form discrete vortex rings. The time-averaged net circulation on the plane depends on the difference between the number of LEVs (n) and TEVs (nk) in the near wake, i.e.

$$\Gamma^- + \Gamma^+ = n(1-k)\Gamma_{\mathrm{LEV}} = n\frac{U_{\mathrm{TEV}} - U_{\mathrm{LEV}}}{U_\infty}\Gamma_{\mathrm{LEV}}. \quad (9)$$

We can now show that the sectional lift computed with eq. 8 is the same as that computed with eq. 6 and 7:

$$-\rho U_\infty(\Gamma^- + \Gamma^+) = -\rho n(U_{\mathrm{TEV}} - U_{\mathrm{LEV}})\Gamma_{\mathrm{LEV}}. \quad (10)$$

This equivalence was also confirmed by the measurements of the streamwise velocity of the LEV by tracking the centroids of the γ_2 isosurfaces in figure 3 and by considering $n = 3$. The convective velocity of the TEV is considered to be U_∞ [14].

The ratio of two between these two velocities matches the approximate ratio of two between Γ^- and Γ^+ showed in figure 4. Therefore, it can be concluded that when the sail is depowered (from $\eta = 0^\circ$ to $\eta = -10^\circ$), the sectional lift decreases almost uniformly along the span of the sail because of a lower circulation of the leading edge vortices, whilst near the sail, they convect downstream always at about half of the free steam velocity.

4.6. Vorticity production

Both in §4.4 and §4.5 we transformed the vortex ring production term in eq. 5 into an equivalent vortex ring growth term. Here we show that a similar force result can be achieved by considering the vortex ring production term directly. In fact, $\dot{\Gamma}$ can be estimated from the vorticity flux through the leading and trailing edge shear layers. Figure 2 shows the two segments L_{LE} and L_{TE}. The first one extends from the surface of the sail in the y direction and has a length $0.3c_0$. The latter is $0.1c_0$ downstream of the trailing edge and has a length of $0.1c_0$ The dimension of L_{TE} is such to avoid inclusion of negative vorticity from either the leading edge or the vertical strut holding the model. Vorticity is not included below the noise threshold. The vorticity fluxes are computed as

$$\dot{\Gamma}_{\mathrm{LE}} = \int_{L_{\mathrm{LE}}} u_x \omega_z dy, \quad (11)$$

$$\dot{\Gamma}_{\mathrm{TE}} = \int_{L_{\mathrm{TE}}} u_x \omega_z dy. \quad (12)$$

Results are shown in figures 5a and 5b for $\eta = 0^\circ$ and $\eta = -10^\circ$, respectively. The differences between the magnitude of the vorticity production at the leading and trailing edge are within the experimental uncertainty. When the sail is eased for strong wind conditions, the nondimensional vorticity production decreases on every spanwise section.

The lift force can be estimated from the vortex ring circulation production, which we found to be $\dot{\Gamma} \approx -\dot{\Gamma}_{\mathrm{LE}} \approx -\dot{\Gamma}_{\mathrm{TE}}$. The area of the vortex ring is the sail itself, and for the lift component of the force we consider only the area projection orthogonal to the lift direction. Hence, for each sail section along the span, the width of the vortex ring is $c\cos\alpha$, where c is the sectional chord length. Finally, assuming that most of the circulation is generated by horizontal shear layers at the leading and trailing edge, eq. 5 can be written as

$$L = \rho \int_S c\cos\alpha\, \dot{\Gamma}\, dz. \quad (13)$$

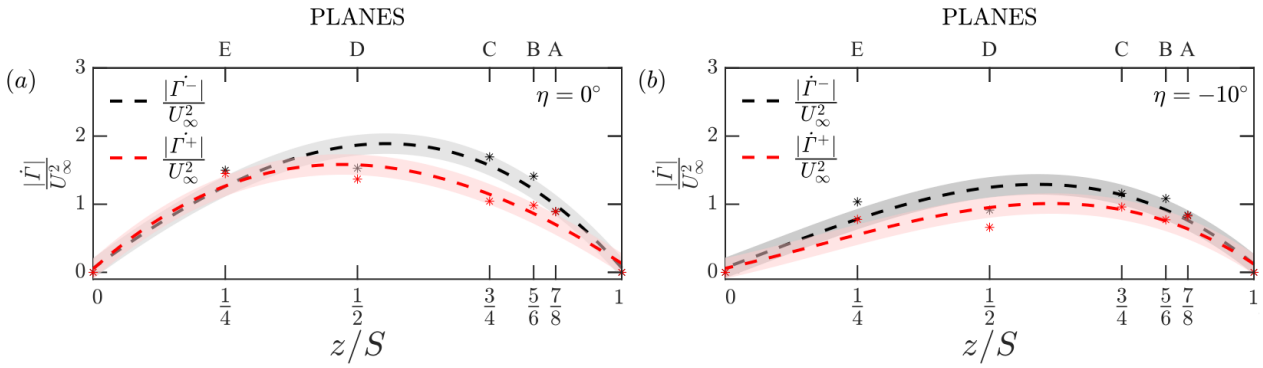

Figure 5 Nondimensional leading-edge circulation production $\left|\dot{\Gamma}_{LE}/U_\infty^2\right|$ and trailing-edge circulation $\left|\dot{\Gamma}_{TE}/U_\infty^2\right|$ versus the spanwise nondimensional coordinate z/S for (a) $\eta = 0^\circ$ and (b) $\eta = -10^\circ$. Markers indicate measured data, whilst dotted lines are third-order polynomial fits with shaded regions showing the 95% CI of the fit.

In Eq. 13, α is the angle between the chordline of the sail's cross-section and the horizontal axis, as shown in Figure 1b. By using the values of $\dot{\Gamma}$ in figure 5 the lift is 12% and 10% higher than that measured with the load cells for $\eta = 0^\circ$ and $\eta = -10^\circ$, respectively.

4.7. Drag

The time-averaged drag can be estimated using Taylor's formula, found in Bryant et al. [23], where it is defined as

$$D = \int_W (p - p_0) dy. \tag{14}$$

This expression states that the drag is the integral over a line W intersecting orthogonally the wake, of the difference between the pressure in the wake p and that in the far field p_0. By using the Bernoulli equation, this equation shows that the drag is equal to the momentum loss in the wake. Wu [24] recently showed that the first order approximation of Eq. 14 is

$$D = \rho U_\infty Q, \tag{15}$$

where, in 2D,

$$Q = \int_W -y\omega_z dy. \tag{16}$$

This enables the use of Taylor's formula by knowledge of only the vorticity field along W and the expression is referred to as the Filon's drag formula. A 2nd order polynomial is utilised to approximate the spanwise distribution of Q. By utilising Eq. 16 and integrating Q along the span of the sail, the steady-state drag coefficient is computed to be C_D = 0.4 and 0.26 for the light wind conditions ($\eta = 0^\circ$) and the strong breeze condition ($\eta = -10^\circ$), respectively.

These values lie within 15 to 20%, respectively, of the drag force coefficients measured with the load cells. The discrepancy is possibly due to the five plane data availability in the spanwise direction and to the effect of vorticity diffusion. We note that the drag of the strut and the rig were measured separately and subtracted to the force measurements, and so the strut and the rig were not the reasons for the discrepancy.

When the sail is depowered from $\eta = 0^\circ$ to $\eta = -10^\circ$, the drag decreases. Interpreting this reduction through Eq. 16, allows the use of figure 2 to identify how a reduction in vorticity enables drag reduction along the span of the sail. By decreasing the angle of attack, the width of the wake on the highest planes A and B decreases significantly, resulting in a lower drag generation. Conversely, the same angle of attack reduction on the lower sections, has a comparatively smaller effect on the wake width and thus on the drag generation.

5. FULL-SCALE SAILS CONSIDERATIONS

Firstly, we recognize that the motion of the flying shape and motion of the boat on the stability of the vortex rings are important considerations that need to be addressed in future research. Secondly, the LEVs and TEVs identified in this paper are fully turbulent and a further increase in the Reynolds number and of the turbulent intensity could enhance mixing and result in smaller vortices. However, their dynamics and the force generation mechanisms are not expected to significantly change. It is noted that that at the low Reynolds number at which we tested, the boundary layer forming from the stagnation points on the sail could be laminar while it would be most likely turbulent at full scale conditions. However, because we showed that the circulation associated with the vorticity in the boundary layer is negligible compared to the free circulation in the bulk flow field, it is unlikely that this would make a significant difference on the flow field. Lastly, at higher Reynolds number and turbulence intensity, we might expect enhanced mixing and consequent lower coherence of the vortex structures and, in turn, lower effectiveness of the different stabilising mechanisms of the leading-edge vortex. For example, the vorticity extraction through axial flow within the core of the leading-edge vortex might be lower at much higher Reynolds numbers than those tested in this work.

6. CONCLUSIONS

We presented force and flow measurements on a spinnaker in a water tunnel to analyse the force generation mechanisms. We considered the sail trim enabling the maximum driving force and a depowered trim. Using particle image velocimetry, we analysed the vorticity fields on five horizontal planes. We observed separated and tridimensional flow, with negligible bound circulation. In contrast, we showed that the vortex dynamics of leading and trailing edge vorticity is the governing force generation mechanism. This was demonstrated by comparing the force derived from the vorticity field with the force measured by the balance.

The vortex force is the rate of change (or the time derivative) of the impulse of a vortex ring in 3D, or a vortex pair in 2D. The leading and trailing edge vortices are the intersection of two of the legs of the vortex ring with the horizontal plane. We showed that considering the vortex lift from the dynamics (strength and relative velocity) of the leading and trailing edge vortices is mathematically equivalent to measuring the lift with the Kutta-Joukowski formula using the time-averaged vorticity field. Similarly, the drag force can be computed from the time-averaged vorticity field and by applying the Filon's drag formula. Furthermore, we noted that the sail force can also be computed from the vorticity flux at the leading edge and trailing edge, because this is equivalent to the production of circulation that feeds the vortex rings that emerge from the perimeter of the sail.

These results demonstrate the theoretical considerations made by Viola et al. [1]. They also pave the way to the development of design methodologies for sails that operate in separated flow conditions, where potential flow approaches are not suitable. The design can be informed by the observation of the local flow field, which can be either measured or computed with, for example, a Navier-Stokes code. Understanding the force generation mechanisms associated with the free vorticity in the field will enable tailoring the vorticity dynamics by design to achieve the desirable aerodynamic force.

Acknowledgements

This work was supported by Consejo Nacional de Ciencia y Tecnologia (CONACYT) with grant number 384490.

References

1. Viola I. M., Arredondo-Galeana, A., Pisetta, G., (2020), "How sails generate forces.", Proceedings of the 5th *Innov'sail Conference*, Gothenburgh, Sweden, June 2020, 1-16.
2. Arredondo-Galeana, A. & Viola, I. M. (2018), "The leading-edge vortex of yacht sails.", *Ocean Engineering*, 159, 552-562.
3. Viola I. M., Arredondo-Galeana, A. (2017), "The leading-edge vortex of yacht sails.", Proceedings of the 4th *Innov'sail Conference*, Lorient, France, June 2017, 115-126.
4. O'Farrell, C., & Dabiri, J. (2014), "Pinch-off of non-axisymmetric vortex rings.", *JFM,* 740, 61-96.
5. Viola, I. M. & Flay, R. G. J. (2009), "Force and pressure investigation of modern asymmetric spinnakers.", *IJSCT Technology Transaction RINA Part B2*, 151(2), 31–40.
6. Viola, I.M. & Flay, R.G.J. (2010), "Pressure distributions on modern asymmetric spinnakers.", *Int. J. Small Cr. Technol.* 152 (B1), 41-50.
7. Viola, I. M., Bartesaghi, S., Van-Renterghem, T. & Ponzini, R. (2014), "Detached Eddy simulation of a sailing yacht." *Ocean Engineering,* 90, 93-103.
8. Bot, P., Viola, I. M., Flay, R. G. J. & Brett, J.-S. (2014), "Wind-tunnel pressure measurements on model-scale rigid downwind sails.", *Ocean Engineering,* 90, 84-92.
9. Perry, AE & Steiner, TR (1987), "Large-scale vortex structures in turbulent wakes behind bluff bodies. Part 1. Vortex formation processes.", *JFM,* 174, 233–270.
10. DeVoria, A. C. & Mohseni, K. (2017), "On the mechanism of high-incidence lift generation for steadily translating low-aspect-ratio wings.", *JFM* 813, 110–126.
11. Kutta, W. M., (1902), "Auftriebskräfte in strömenden flüssigkeiten.", *Illust. Aeronaut. Mitt*.
12. Jowkowski, N. E., (1906)y, "On annexed vortices.", *Proc. Phys. Sect. Nat. Sci. Soc.,* 13 (2), 12-25.
13. Graftieaux, L., Michard, M. & Grosjean, N. (2001), "Combining PIV, POD and vortex identification algorithms for the study of unsteady turbulent swirling flows." *Meas Sci Technol* 12 (1201), 1422–1429.
14. Stevens, P. R. R. J., Babinsky, H., Manar, F., Mancini, P., Jones, A. R., Granlund, K. O., Nakata, T., Phillips, N., Bomphrey, R. J. & Gozukara, A. C. (2016), "Low Reynolds Number Acceleration of Flat Plate Wings at High Incidence (Invited).", *In 54th AIAA Aerosp. Sci. Meet. AIAA SciTech Forum*, (AIAA 2016-0286), pp. 1-15.
15. Wu, J. C. (1981), "Theory for aerodynamic force and moment in viscous flows." *AIAA Journal,* 19 (4), 432-441.
16. Lighthill, J. (1986), *An Informal Introduction to Theoretical Fluid Mechanics*, Clarendon Press, UK.
17. Eldredge, J. D. (2019), *Mathematical Modelling of Unsteady Inviscid Flows*, Springer, Switzerland.
18. Koumoutsakos, P. & Leonard, A. (1995), "High-resolution simulation of the flow around an

impulsively started cylinder using vortex methods*.", JFM,* 296, 1-38.

19. Leonard, A & Roshko, A (2001), "Aspects of flow-induced vibrations*.", J. Fluids Struct*., 15, 415-425.
20. Rival, D. E. & van Oudheusden, B. (2017), "Load-estimation techniques for unsteady incompressible flows.", *Exp. Fluids*, 58 (3), 1-11.
21. Lentink, D. (2018), "Accurate fluid force measurement based on control surface integration.", *Exp. Fluids,* 59 (1), 1-12.
22. Lamb, H. (1932), *Hydrodynamics*. Cambridge University Press.
23. Bryant, L. W., Williams, D. H., Taylor, G. I. & Bairstow, L. (1926), "An investigation of the flow of air an aeorofoil of infinite span.", *Philosophical Transactions of the Royal Society of London, Series A, Containing Papers of Mathematical or Physical Character,* 225 (626-625), 199-245
24. Wu J, Ma H, Zhou M (2006), *Vorticity and vortex dynamics*, Springer, Germany.